

Performance analysis of alternative propellants for a helicon plasma thruster

SPACE PROPULSION 2020+1

17 - 18 - 19 MARCH 2021

J. Zhou¹, F. Taccogna², P. Fajardo³ and E. Ahedo⁴

¹Equipo de Propulsión Espacial y Plasmas, Universidad Carlos III de Madrid, 28911 Leganés, Spain, Email: jzhou@pa.uc3m.es

²Istituto per la Scienza e Tecnologia dei Plasmi, Consiglio Nazionale delle Ricerche

³Equipo de Propulsión Espacial y Plasmas, Universidad Carlos III de Madrid

⁴Equipo de Propulsión Espacial y Plasmas, Universidad Carlos III de Madrid

KEYWORDS:

Helicon plasma thruster simulation, complex chemistry modeling, alternative propellants, air-breathing thruster concept.

ABSTRACT:

HYPHEN, a hybrid particle/fluid two-dimensional asymmetric code, is used for the assessment of alternative propellants to Xe . The modeling of collisions in HYPHEN is described, with special focus on the treatment of diatomic molecules, and for which the most important collisions and species are identified. The code is used to assess the air-breathing concept in helicon plasma thrusters, which has potential use for drag compensation within low orbits, and the prototype HPT05M is used for such evaluation. Simulations are run for N_2 and O , the main components of air within low altitudes. Results of 2D maps and performances are studied and compared with Xe .

1 INTRODUCTION

Xenon has been the most used propellant for electric propulsion (EP). Xe has a good trade-off of properties. First, Xe has a low energy threshold and high cross section for ionization, i.e. ionization requires a small amount of energy and happens frequently, which is important in space due to the limited energy reserves. Second, Xe is a heavy substance, which is beneficial for thrust generation. Third, Xe is chemically inert and the interaction with the components of the thruster is minimized extending its lifetime, which is specially critical for those with electrodes, e.g. Hall Effect Thruster and Gridded Ion Thruster. However, Xe is very scarce in the atmosphere, and the separation from air requires many stages of refrigeration and expansion. An exclusive production of Xe would be very costly and not feasible, and usually it is obtained as a byproduct of oxygen production for industrial uses. Thus, the amount of Xe produced is driven in turn by the

demand of oxygen. EP is growing and substituting the traditional chemical thrusters, and the current offer of Xe will not be able to satisfy the foreseen increasing demand [1, 2].

The search of candidates for alternative propellants is a current topic of interest. Traditionally, other noble gases, e.g. argon and krypton, have been proposed [3]. These are more abundant than Xe in the atmosphere, but are still rare gases that are produced in the same way as Xe and are driven by the oxygen demand. On the other hand, non-noble substances have been investigated as well. Iodine is advantageous from a system point of view, which allows compact storage in solid state and does not need high pressure tanks, and has similar performances compared to Xe [4, 5]. Water, which is abundant in the solar system, would make feasible the concept of in-situ resources utilization for propellant replenishment [6–8]. Novel thrust concepts have also appeared, such as the air-breathing thrusters, which have potential use in low Earth orbits for drag compensation. Since no large propellant storage is needed, this concept would allow long-term missions at low altitudes [9–12]. The non-noble substances, although versatile, are reactive. In this respect, electrodeless thrusters under development such as the Electron Cyclotron Resonance Thruster (ECRT) and the Helicon Plasma Thruster (HPT) are more tolerant and have been tested experimentally with a wide variety of propellants [13–15].

The modeling of thruster operations with complex chemistry, which is necessary for many of the alternative propellants, is not very advanced. The existing thruster models are rather simple ones that are not able to handle mixtures of several substances or molecular collisions such as dissociation, vibrational and rotational excitations, etc. Recently, Sheppard and Little [8] progressed partially on this issue: they developed a one-dimensional model for electrodeless thrusters to characterize properly the complex chemistry and obtained results for operation with water. Being one-dimensional, details such as realistic magnetic topologies, different from a purely axial one, and wall losses are not con-

sidered. Furthermore, electric potential and electron temperature are not solved self-consistently, but are related through a phenomenological relation.

This work presents the modeling with HYPHEN, a multi-thruster simulation code platform with application for a wide variety of thrusters including ECRT and HPT [16, 17]. HYPHEN implements an axisymmetric (two-dimensional) plasma model, and solves self-consistently the main aspects of the discharge. The interaction of the species with different type of surfaces (dielectric, metallic, etc) and complex magnetic topologies can be modeled. HYPHEN can also handle multiple species and has been extended, for this work, to handle collisions typical of diatomic molecules. Simulations are run for the HPT prototype HPT05M using air as propellant, and plasma profiles and operation performances are studied and compared with Xe .

The rest of the work is organized as follows: Section 2 describes the configuration of HPT05M and the structure of HYPHEN, Section 3 explains the implementation of collisions in HYPHEN, Section 4 discusses the simulation results, and Section 5 summarizes the conclusions.

2 GENERAL ASPECTS

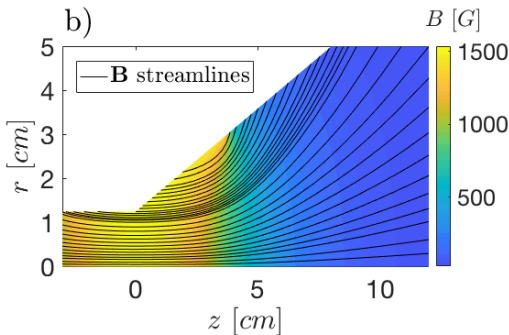
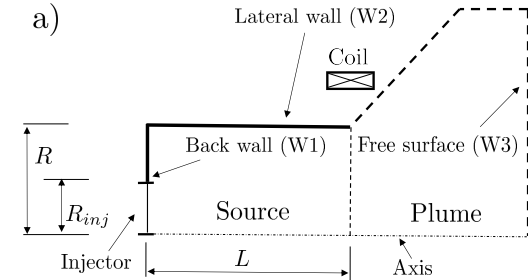


Figure 1: (a) Sketch of the thruster and (b) applied magnetic field generated by the external magnetic circuit.

Figure 1 (a) is a sketch of a particular configuration for the HPT05M prototype. The thruster vessel is made of ceramic material and has radius

$R = 1.25\text{cm}$ and length $L = 3\text{cm}$. An injector of radius $R_{inj} = 0.4\text{cm}$ delivers a mass flow \dot{m} . The external magnetic circuit consists of a coil placed around the vessel exit to generate a stationary magnetic field B . Figure 1 (b) shows the field, which has a convergent-divergent geometry with a throat at the vessel exit.

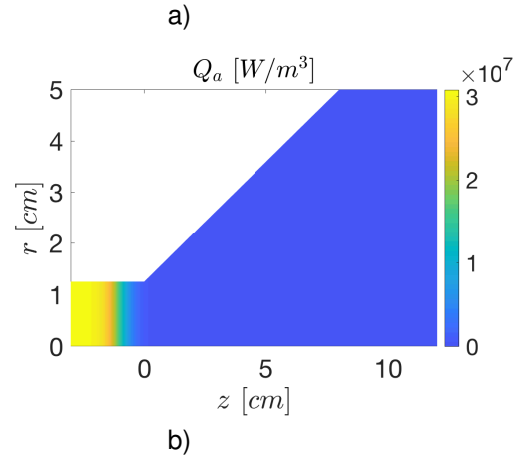
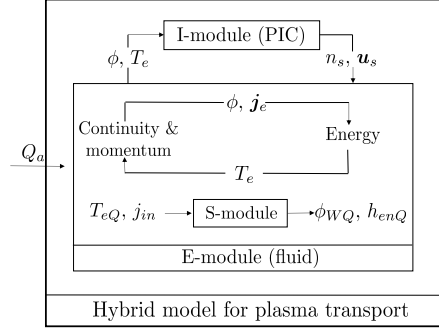


Figure 2: (a) Structure of the code. (b) Power deposition map.

HYPHEN simulates the thruster with a modular code structure: modules are coded separately for different plasma species and physical phenomena, and then these modules are integrated. There are three modules for the plasma transport as seen in Fig. 2 (a): an Ion(I)-module solving for the production and dynamics of a heavy species particle-in-cell (PIC) model; an Electron(E)-module solving for an electron quasi-neutral fluid model; and a Sheath(S)-module solving for the plasma response in the non-neutral discontinuities near the surfaces. In addition, there is a wave(W)-module solving for the plasma wave-interaction, which is not used in the present work. Instead, a given power deposition map Q_a is imposed, which is shown in Fig. 2 (b). The deposition is uniformly distributed inside the vessel to obtain a fixed total deposited power P_a . The I-module and E-module are run sequentially. Let denote n_s and u_s as, respectively, the density and velocity of species s (electrons e , ions i or neutrals n); ϕ and T_e as, respectively, the electric potential and elec-

tron temperature. The I-module gives, as outputs, n_s and \mathbf{u}_s for heavy species. These outputs are taken by the E-module together with the power deposition map. The E-module, and the S-module for wall magnitudes, give a complete solution of ϕ and T_e , which are necessary for a new time advancement of the I-module.

The I-module uses a Cartesian mesh defined on the natural cylindrical reference frame $\{\mathbf{1}_z, \mathbf{1}_r, \mathbf{1}_\theta\}$ as seen in Fig. 3 (a). The E-module uses a magnetic field aligned mesh (MFAM) due to the anisotropic character of the magnetized electron fluid [16]. A MFAM is defined on the magnetic reference frame $\{\mathbf{1}_\perp, \mathbf{1}_\parallel, \mathbf{1}_\theta\}$, $\mathbf{1}_\parallel = \mathbf{B}/B$ and $\mathbf{1}_\perp = \mathbf{1}_\parallel \times \mathbf{1}_\theta$, as seen in Fig. 3 (b).

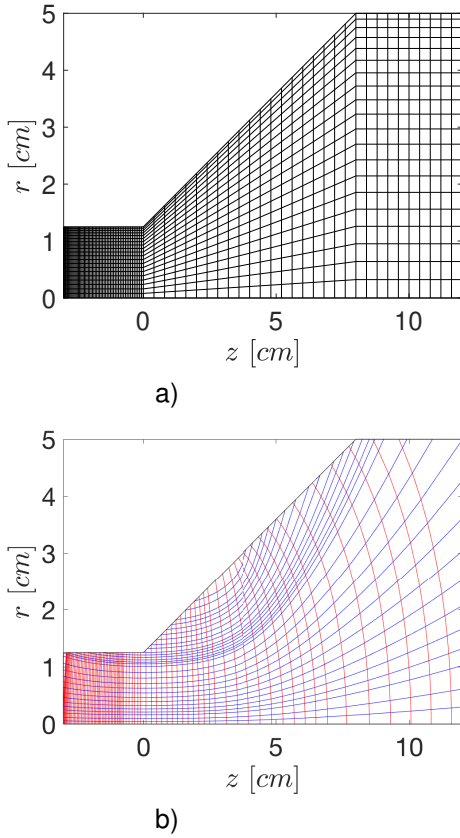


Figure 3: (a) Cartesian mesh of I-module and (b) MFAM mesh of E-module.

2.1 I-module

The I-module solves a PIC model [18, 19]. The module is based on three main algorithms: first, a particle mover propagates the trajectory of the macroparticles with a leap-frog scheme; second, a collision operator performs the interaction between the macroparticles and with the electron fluid; third, a wall interaction operator solves for ion recombination, neutral accommodation, and forces the fulfillment of the Bohm condition in the walls. The model allows the treatment of species in separate computational lists, which make flexible the handling of a

high number of species at the same time and the interaction between them. The number of macroparticles of each list in each cell is regulated with a statistical population control, which is beneficial for noise reduction and computational efficiency.

2.2 E-module

The electron fluid is described with a magnetized, weakly-collisional and drift-diffusive (inertial-less) model [19, 20]:

$$n_e = \sum_{s \neq e} Z_s n_s, \quad (\text{Eq. 1})$$

$$\nabla \cdot \mathbf{j} = \nabla \cdot (\mathbf{j}_e + \mathbf{j}_i) = 0, \quad (\text{Eq. 2})$$

$$0 = -\nabla(n_e T_e) + en_e \nabla \phi + \mathbf{j}_e \times \mathbf{B} + \mathbf{F}_{res} + \mathbf{F}_{turb}, \quad (\text{Eq. 3})$$

$$\frac{\partial}{\partial t} \left(\frac{3}{2} n_e T_e \right) + \nabla \cdot \mathbf{h}_e = -\nabla \phi \cdot \mathbf{j}_e + Q_e + Q_a, \quad (\text{Eq. 4})$$

$$0 = -\frac{5n_e T_e}{2e} \nabla T_e - \mathbf{q}_e \times \mathbf{B} - \frac{5T_e}{2e} (\mathbf{F}_{res} + \mathbf{F}_{turb}) - \frac{m_e \nu_e}{e} \mathbf{q}_e + \mathbf{Y}_{turb}. \quad (\text{Eq. 5})$$

Equation 1 is the quasi-neutrality condition, where Z_s is the charge number of species s , and allows to obtain density of electrons through the densities of heavy species. Equation 2 is the conservation of current density $\mathbf{j} = \mathbf{j}_e + \mathbf{j}_i$, where $\mathbf{j}_e = -en_e \mathbf{u}_e$ is the electron current density and $\mathbf{j}_i = e \sum_{s \neq e} Z_s n_s \mathbf{u}_s$ is the ion current density, and the plasma beam is current-free since no current source exits. [The current density vectors can be divided in the azimuthal and longitudinal current densities, i.e. $j_{\theta s} = \mathbf{j}_s \cdot \mathbf{1}_\theta$ and $\hat{\mathbf{j}}_s = \mathbf{j}_s - j_{\theta s} \mathbf{1}_\theta$.] Equation 4 is the energy conservation. On the left-hand side, there is total variation of energy: temporal derivative and total energy flux, which is $\mathbf{h}_e = T_e n_e \mathbf{u}_e 5/2 + \mathbf{q}_e$ with \mathbf{q}_e the heat flux. On the right-hand side, the energy changes with: work of electric field $-\nabla \phi \cdot \mathbf{j}_e$ and inelastic collisions Q_e .

Equation 3 is for momentum and there is a balance among: pressure gradient $-\nabla(n_e T_e)$; electric field $en_e \nabla \phi$; magnetic force $\mathbf{j}_e \times \mathbf{B}$; collisional resistive force $\mathbf{F}_{res} = -\sum_{s \neq e} \nu_{es} m_e n_e (\mathbf{u}_e - \mathbf{u}_s)$, ν_{es} the collision frequency with species s ; and an anomalous transport force due to turbulence \mathbf{F}_{turb} . Equation 5 is for heat flux and has dual terms compared with the momentum equation. Here, two collision terms are present, $-\mathbf{F}_{res} 5T_e/2e$ corresponds to the resistive force from the momentum equation, and $\mathbf{q}_e m_e \nu_e/e$ is the direct effect of collisions on the heat flux with $\nu_e = \sum_{s \neq e} \nu_{es}$ the total electron collision frequency; and contributions of turbulence are also included, $-\mathbf{F}_{turb} 5T_e/2e$ and \mathbf{Y}_{turb} . The turbulence terms are modeled with phenomenological models [21, 22] as $\mathbf{F}_{turb} = \alpha_t j_{\theta e} B \mathbf{1}_\theta$ and $\mathbf{Y}_{turb} =$

$-\alpha_t q_{\theta e} B \mathbf{1}_{\theta}$, which enhance, respectively, the electron current and heat flux across the magnetic field lines. The parameter α_t has to be selected and, based on typical values in the literature, is taken as $\alpha_t = 0.01$.

Boundary conditions and plasma-wall interaction (S-module)

The boundary conditions are set on the currents and total energy fluxes normal to the surfaces: $j_n = \mathbf{j} \cdot \mathbf{n}$ and $h_{en} = \mathbf{h}_e \cdot \mathbf{n}$ with \mathbf{n} the outward unit normal. On the axis, symmetry implies that $j_n = 0$ and $h_{en} = 0$. On the ceramic walls, the dielectric condition $j_n = 0$ is applied and h_{en} comes from the sheath model. On the free surface, the current-free condition states that $\int_{W_3} j_n dS = 0$. The condition can be fulfilled simply as $j_n = 0$ without significant influences on the simulation results if the free surface is far enough as seen in Ref. [16]. Regarding the total energy flux, kinetic studies [23] suggest that $h_{en} = cn_e T_e u_{en}$ with c a constant taken as $c = 9/2$. The S-module relates plasma magnitudes at the quasi-neutral edge Q and the ceramic walls of the vessel W . The model implemented is from Ref. [24], which is collisionless and unmagnetized, i.e. Debye length is much smaller than the mean free path and Larmor radius, and accounts for two populations of electrons: (i) primary electrons from the plasma bulk and (ii) secondary electrons emitted from the ceramic material. In addition, for primary electrons, the elastically reflected and repletion of high energy tail particles are considered as well. The outputs of the model are the potential drop and the total energy flux through the sheath,

$$\frac{e\phi_{WQ}}{T_{eQ}} = \ln \left[\frac{en_e \sqrt{\frac{8T_e}{\pi m_e}}}{4j_{in}} \right]_Q \sigma_t (1 - \delta_{wr}) (1 - \delta_{ws}), \quad (\text{Eq. 6})$$

and

$$h_{enQ} = 2T_{eQ} \frac{j_{in}/e}{1 - \delta_{ws}} - 2T_s \delta_{ws} \frac{j_{in}/e}{1 - \delta_{ws}} + \phi_{WQ} j_{in}, \quad (\text{Eq. 7})$$

respectively. In these expressions, δ_{ws} is the fraction of secondary electrons emitted from the wall with a temperature T_s , which is taken as $T_s = 2eV$ (usually cold); and δ_{wr} is the same but for elastically reflected primary electrons. These yields depend on T_e and are modeled as

$$\delta_{wr} = \delta_{r0} \frac{E_r^2}{(T_{eQ} + E_r)^2}, \quad \delta_{ws} = \frac{2T_{eQ}}{E_s}, \quad (\text{Eq. 8})$$

where the parameters δ_{r0} , E_s and E_r depend on the type of ceramic material. Taking the common Boron Nitride, we have that $\delta_{r0} = 0.4$, $E_s = 50eV$ and $E_r = 20eV$ [24, 25]. Finally, σ_t is the replenishment fraction of the primary electron high energy tail, which changes usually in the range $\sigma_t \sim 0.1-0.3$ and is taken as $\sigma_t = 0.1$.

3 MODELING OF COLLISIONS

3.1 Type of collisions

In low altitudes, where the air-breathing concept can be applied, the main components of air are N_2 and O [26]. From sea level until 200km, the composition is dominated by N_2 , and from 200km until 400km, by O . The modeling of atomic substances are common and well-known, and the discussion is focused on diatomic substances, which is the novel part implemented in HYPHEN.

Table 1 shows the collisions for simulations with diatomic substances. The formula of each collision is given for a generic substance, where A_2 stands for a diatomic molecule and A for an atom, and superscript $+$ refers to positive ions and e to electrons. Only electron-heavy species collisions are considered, while the heavy-heavy species and photon-driven ones are negligible within the normal operation conditions in EP. The electrons, if energetic enough, can ionize and also dissociate the diatomic molecules through collisions, thus producing molecular ions A_2^+ and atoms A . Instead, the electrons without enough energy excite A_2 , and the excitation accounts for the transitions between electronic states, and also for those between vibrational and rotational states. Apart from the inelastic collisions, the electrons can collide elastically with A_2 and through Coulomb interaction with A_2^+ . The derived species A from dissociation suffers collisions as well being possible again the ionization to produce A^+ , the excitation, and the elastic collisions. Although excitation collisions are considered, we assume that the excited neutrals decay immediately, so that the only neutrals tracked in the simulations are those on ground state.

Type of collision	Formula
Elastic	$A_2 + e \rightarrow A_2 + e$
Coulomb	$A_2^+ + e \rightarrow A_2^+ + e$
Excitation	$A_2 + e \rightarrow A_2^* + e$
Ionization	$A_2 + e \rightarrow A_2^+ + 2e$
Dissociation	$A_2 + e \rightarrow 2A + e$
Elastic	$A + e \rightarrow A + e$
Coulomb	$A^+ + e \rightarrow A^+ + e$
Excitation	$A + e \rightarrow A^* + e$
Ionization	$A + e \rightarrow A^+ + 2e$

Table 1: Type of collisions considered when simulating for diatomic molecules.

The collision i is characterized with a reaction rate R_i , which is, for negligible heavy species velocity and an electron Maxwellian distribution of tempera-

ture T_e ,

$$R_i(T_e) = \sqrt{\frac{8}{\pi m_e T_e^3}} \int_{\varepsilon_{th,i}}^{\infty} \varepsilon_e \sigma_i(\varepsilon_e) \exp(-\varepsilon_e/T_e) d\varepsilon_e. \quad (\text{Eq. 9})$$

Here: ε_e is the electron impact energy, $\varepsilon_{th,i}$ is the threshold energy of the reaction, and σ_i is the cross section. The threshold energy is the one needed each time a collision of the reaction happens. The elastic and Coulomb reactions have $\varepsilon_{th,i} = 0$, and the rest (ionization, excitation and dissociation) are inelastic reactions, with $\varepsilon_{th,i} > 0$, which involve energy losses. The cross section of the reaction, σ_i , is a function of ε_e , and data determined experimentally or theoretically is available in the literature. The rate measures the likelihood for a reaction to happen, and physically represents the volume swept by an electron in its trajectory. The rate multiplied by the density of the collision target heavy species s gives the collision frequency $\nu_{es} = n_s R_{es}$. Data of cross sections for low-temperature plasmas have been collected for N_2 , N and O . There are data from journal articles specific for the topic [27–30], where compilations are done; detailed quantum mechanics computations [31, 32], and the online database LXCAT [33, 34]. The information is repeated over the different sources, and is postprocessed with a benchmark before being used in HYPHEN.

	N_2	N	O	Xe
$\varepsilon_{th,ion}$	15.6	14.8	13.6	12.1
$\varepsilon_{th,elec-exc}$	~ 10	~ 8	~ 8	~ 8
$\varepsilon_{th,vib-exc}$	≈ 0	-	-	-
$\varepsilon_{th,rot-exc}$	≈ 0	-	-	-
$\varepsilon_{th,diss}$	9.8	-	-	-

Table 2: Threshold energy [eV] of reactions for air substances, Xe is shown for comparison.

Figure 4 and Table 2 shows, respectively, the rates versus T_e and the energy thresholds, for air substances and Xe . The notation used for the collisions are: elastic collision (en), Coulomb collision (ei), ionization (ion), electronic excitation ($elec - exc$), vibrational excitation ($vib - exc$), rotational excitation ($rot - exc$), and dissociation ($diss$). The rate for Coulomb collision does not come from the sources mentioned above, but from a general analytical formula known from plasma theory [35]. The excitation rates include the transitions from ground state to the relevant states that have been identified. Notice that each transition from ground state to a higher energy state has a different threshold, and the values shown are averaged ones for the temperature range of interest ($\sim 10eV$) in EP. One of the main objectives in an EP device is to try to fully ionize the propellant. Xe has a ε_{ion} slightly smaller, and R_{ion} 2-3 times larger than N_2 and O . In N_2 , the ionization can happen as separate dissociation-ionization,

but this indirect way is more costly in terms of energy. The excitations imply energy losses and have to be minimized: the electronic excitation thresholds are comparable to the ionization ones. In N_2 , there are vibrational and rotational excitations additionally, which however have $\varepsilon_i \approx 0$ and are basically elastic collisions. The dominance of R_{ion} over R_{exc} , happens if electron temperature is high enough: about $10eV$ for Xe and O , and $20eV$ for N_2 .

3.2 Implementation in HYPHEN

The plasma properties change along the discharge while the species collide between them. The collisions modify the plasma via species production, momentum transfer and power losses. In the hybrid formulation and quasi-neutral plasma approach of HYPHEN, the I-module is in charge of the generation of species. The momentum transfer and power losses are assigned to the E-module for electrons due to the large mass disparity with respect to heavy species.

I-module

The collisions that generate species are ionization and dissociation. The former, as obvious, was already implemented in HYPHEN, and here the algorithms are generalized to handle also the latter. The generation is done for each mesh cell and per each time step of the I-module. First, the total mass of the new species to be generated is obtained as

$$\Delta m = m_s n_s n_e R_{es}(T_e) V \Delta t, \quad (\text{Eq. 10})$$

where: V is the cell volume and Δt the time step. Second, the amount of macroparticles to be generated is given by

$$N_p = \frac{\Delta m}{m_s W_{gen}}, \quad (\text{Eq. 11})$$

with W_{gen} the generation weight selected, i.e. the number of elementary particles within one macroparticle. In ionization, N_p is exactly the number of new macroparticles, but in dissociation, there are N_p pair of macroparticles.

The new generated macroparticles, apart from their weights, need to be assigned a position and a velocity. The position of the macroparticles is allocated randomly with an uniform probability inside the cell where they are generated. Regarding the velocity, the procedure is different for ionization and dissociation. For ionization and each of the N_p new macroparticles, we sample a velocity of the original species from a Maxwellian distribution defined with the local properties, namely v_s , and which is allocated directly. For dissociation, the same sampling is done for each N_p pair of new macroparticles, but now v_s has to be distributed over the pair. The distribution is done in a way so that the output species

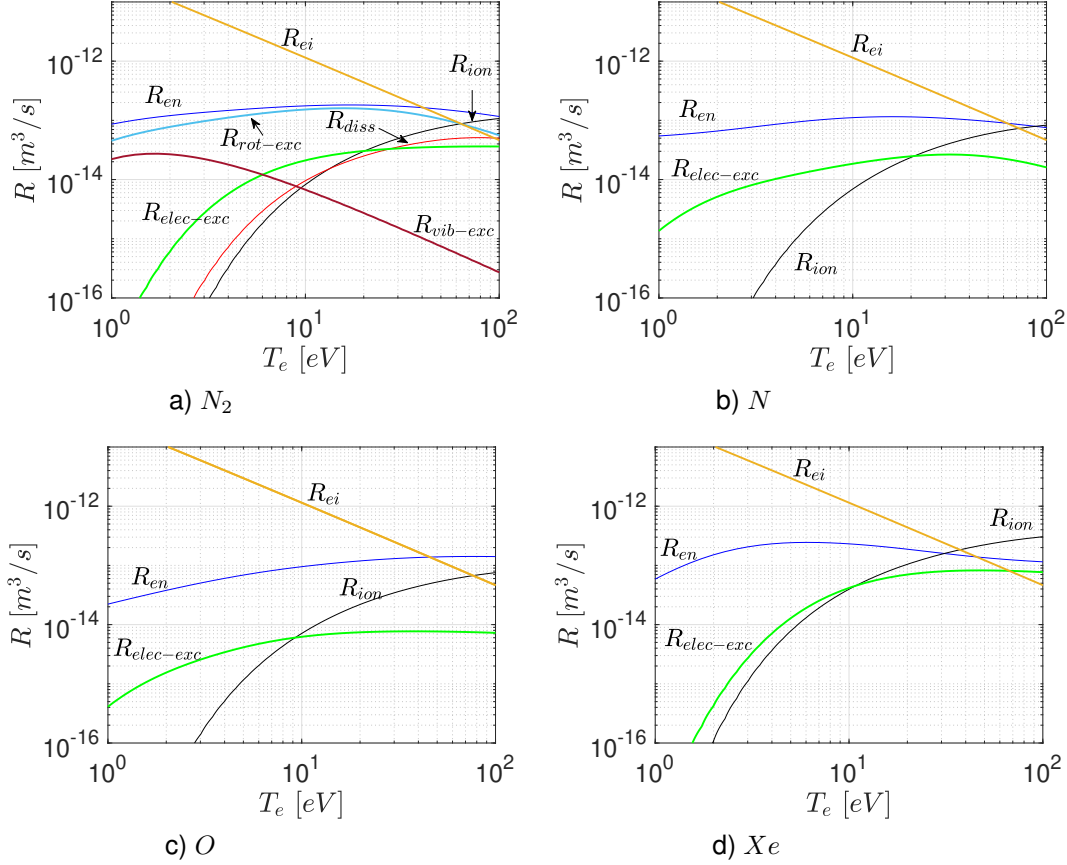


Figure 4: Reaction rates of air substances, Xe is shown for comparison.

conserved the energy of the input ones. The output velocities have modules

$$|v_1| = \sqrt{2(1-x)}|v_s|, \quad |v_2| = \sqrt{2x}|v_s|, \quad (\text{Eq. 12})$$

where x is a random number chosen uniformly between 0-1, and directions uniformly distributed over the space.

E-module

In the fluid model of E-module, the collisions contribute to momentum (Eq. 3) and energy (Eq. 4), and more specifically to, respectively, the collision resistive force F_{res} and power losses:

$$Q_e = -n_e \sum_{s \neq e} v_{es} \varepsilon_{th,es}. \quad (\text{Eq. 13})$$

4 RESULTS

Simulations are run separately for N_2 and O . The propellants are evaluated operating with a propellant mass flow of $\dot{m} = 1 \text{ mg/s}$ and a total power deposited $P_a = 300 \text{ W}$.

4.1 2D plasma profiles

The 2D plasma profiles for N_2 and O are displayed in Figs. 5 and 6. Panels (a) show the electron temperature, and profiles isothermal along the magnetic field lines and radially decaying are found. Panels (b)-(c) show the neutral and plasma densities: the propellant is partially depleted, and the ionization is poor ($n_e \ll n_{N_2}, n_O$). In the case of N_2 , there is also dissociation, which is important since we have $n_{N_2} \sim n_N$ as seen in panel (g). The generation of electrons come from ionization of both N_2 and N , panels (h) and (i) show the densities of $n_{N_2}^+$ and n_N^+ , and they are comparable. Panels (d) show the potential, with a peak inside the vessel around $(z, r) = (1.5, 0.8) \text{ cm}$, and decays in all directions. Panels (e)-(f) show the longitudinal ion velocity and current density. We see that ions follow the potential fall: a part of the ions hit and are recombined in the vessel walls, and another part exit the vessel and are accelerated to supersonic conditions to generate thrust.

The analogous plots for Xe are shown in Fig. 7. The comparison reveals that the general physics for N_2 and O are similar to that of Xe . The main difference is that the electron temperature is larger for Xe [panels (a)] and, with a higher level of ionization, the propellant is ionized nearly in totality [panels (b)-

(c)]. The potential falls are accordingly higher [panels (d)], and the ion acceleration is milder [panels (e)] since Xe is heavier. The electron heating is related to the plasma wall recombination. The power losses are proportional to j_i/eT_e on the wall and since the total deposited power is fixed, the higher j_i/e , the lower T_e . This is proved indeed in the ion fluxes of panels (f), where more recombination is observed for N_2 and O than for Xe , and therefore the magnetic confinement plays a key role. The electron azimuthal current density, $j_{\theta e}$, produces a force $-j_{\theta e}B\mathbf{1}_{\perp}$, which, inside the vessel, given the nearly axial magnetic topology ($\mathbf{1}_{\perp} \approx \mathbf{1}_r$), screens the plasma from the walls. There is worse confinement for N_2 and O due to the larger level of collisionality: given the same amount of propellant mass flow, more particles for N_2 and O are present since they are lighter [panels (b)-(c)], and thus more collisions take place. Fig. 8 compares $j_{\theta e}$ and electron collision frequency ν_e for the propellants, and corroborate the argument.

4.2 Performances

Table 3 shows the performance indicators (which are defined in Appendix A) of the HPT operated with N_2 and O . The analogous results for Xe are shown for comparison. Apart from the deposited power $P_a = 300W$, we also show the results for $P_a = 600W$. Xe offers better overall efficiency, η_F (notice that $\eta_F = \eta_u\eta_{ene}\eta_{disp}$), than N_2 and O as expected. Operating with $P_a = 300W$, N_2 and O have a η_F of 1.3-4.5%, which are noticeably worse than the 10.4% of Xe . The poor performance is due to the poor electron heating: the volumetric mean temperature, $\langle T_e \rangle$, is 4.84-5.19eV for N_2 and O , while Xe has 25.35eV. In consequence, there is a low propellant utilization, N_2 and O have a plume partially ionized, $\eta_u = 20$ -34%. Furthermore, the portion of power carried by the plume (useful for thrust) is worse as well, $\eta_{ene} = 16$ -35%. The energy balance suggests that the larger power losses are due to inelastic collisions, $\varepsilon_{inel} = 44$ -69%, which are dominated by the excitation.

Introducing more power, $P_a = 600W$, $\langle T_e \rangle$ grows accordingly. The increment is noticeable for Xe , and small for N_2 and O . In Xe , the efficiencies remain similar and thrust is increased. In N_2 and O , the propellant utilization is nearly double, and the portion of beam power is slightly improved. The overall efficiency follows η_u and is increased to $\eta_F = 2.4$ -7.6%. If further power is deposited and $\langle T_e \rangle$ is high enough to have full ionization ($\eta_u \approx 1$), we can expect, based on the tendency observed, to achieve $\eta_F \sim 5$ -10%. Then for high powers, air would have efficiencies comparable to those of Xe .

Since the simulations have been run separately for N_2 and O , the performances of air as mixture, within the first 400km of the atmosphere, are expected to

be a kind of average between them. Results suggest that O presents a better performance than N_2 , thus thrust efficiency would increase with altitude.

5 CONCLUSIONS

The search of alternative propellants for EP is a current topic due to the scarce supply for Xe and the foreseen growth of EP. Several candidates have been proposed with potential advantages. However, many of them have molecular structures, and there was no simulation tool that, at the same time, reproduces self-consistently the physics of the plasma discharge and models complex chemistry. The simulation code HYPHEN fills that gap and contributes to a progress. The code has been extended to include collisions typical of diatomic molecules, which already allows to assess a wide variety of propellants. The tool is used to evaluate air as alternative propellant, which is the basis for air-breathing concepts. The HPT05M prototype is used for the simulations.

Simulations are run considering low altitudes, where the air is still dense enough. Within the first 400km, the air is dominated by N_2 (0-200km) and O (200-400km), and N_2 and O are evaluated separately. The results of 2D maps and performances are shown and compared with Xe . Studies reveal that the main 2D profiles and physical mechanisms of the discharge are similar. The main difference is that the electron heating is less effective for N_2 and O given the same amount of deposited power. This is due to a worse confinement for them: for the same mass flow of propellant and being less massive, their particle densities are larger and therefore they are more collisional. At low power ($\sim 100W$), the low electron temperature, makes the plume poorly ionised and they have a thrust efficiency far from that of Xe . At high power ($\sim 1000W$) however, for which the temperature is enough, they could be competitive with respect to Xe . Furthermore, O is found to have better efficiency than N_2 , and then higher altitudes of flight are better in terms of propulsive performance.

A PERFORMANCE INDICATORS

The thrust produced in the plasma discharge satisfies

$$F = \int_{W3} \sum_s (n_s m_s u_{zs} \mathbf{u}_s \cdot \mathbf{n} + n_s T_s \mathbf{1}_z \cdot \mathbf{n}) dS, \quad (\text{Eq. 14})$$

i.e. the momentum flow over the free surface W3 (see Fig. 1), and includes dynamic and static components. Notice that the sign criterion considered is $F > 0$ for a propelling force, and $F < 0$ for a drag force. It accounts for all the species, and the contribution of heavy species is computed with the

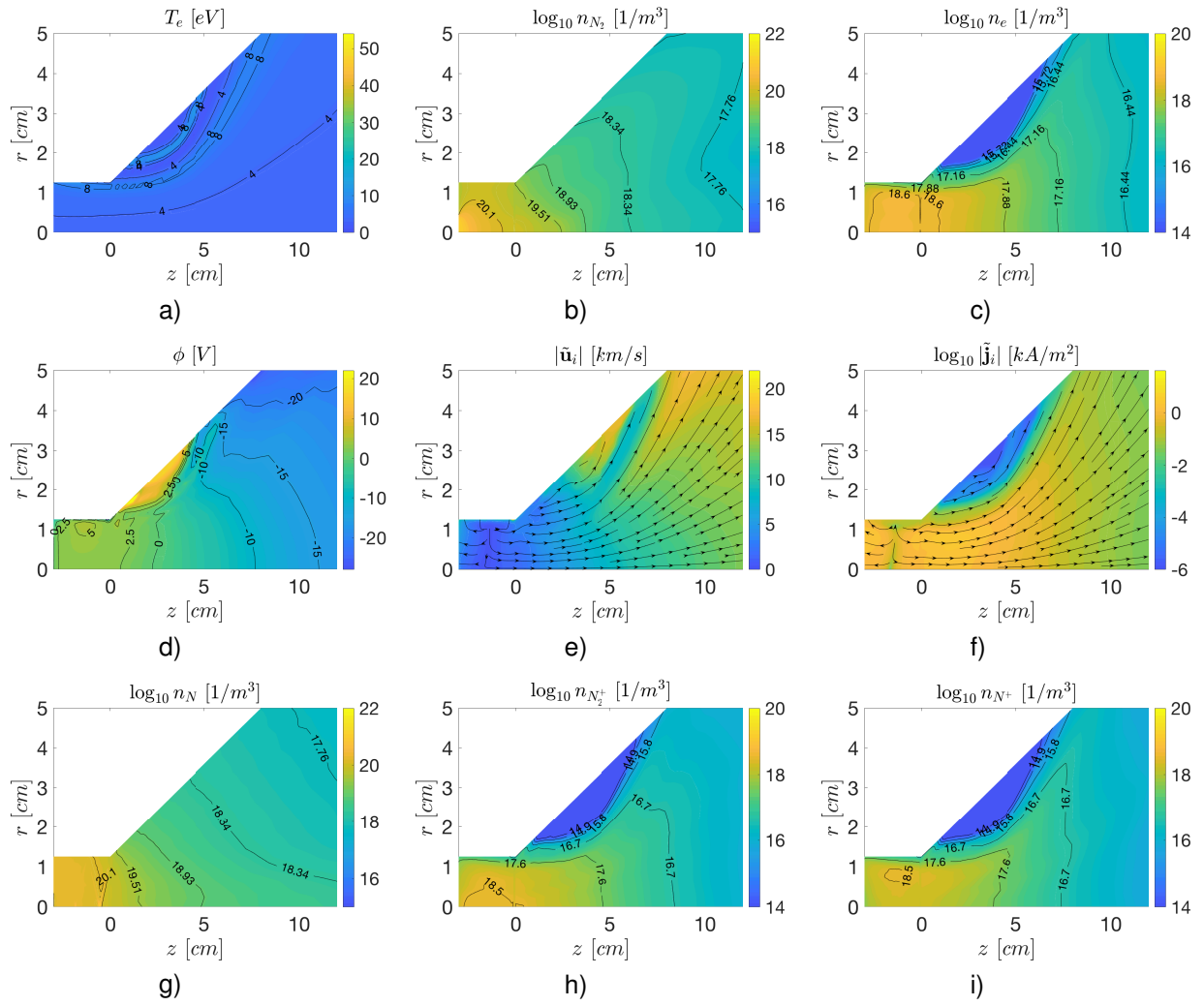


Figure 5: 2D maps of plasma magnitudes for N_2 .

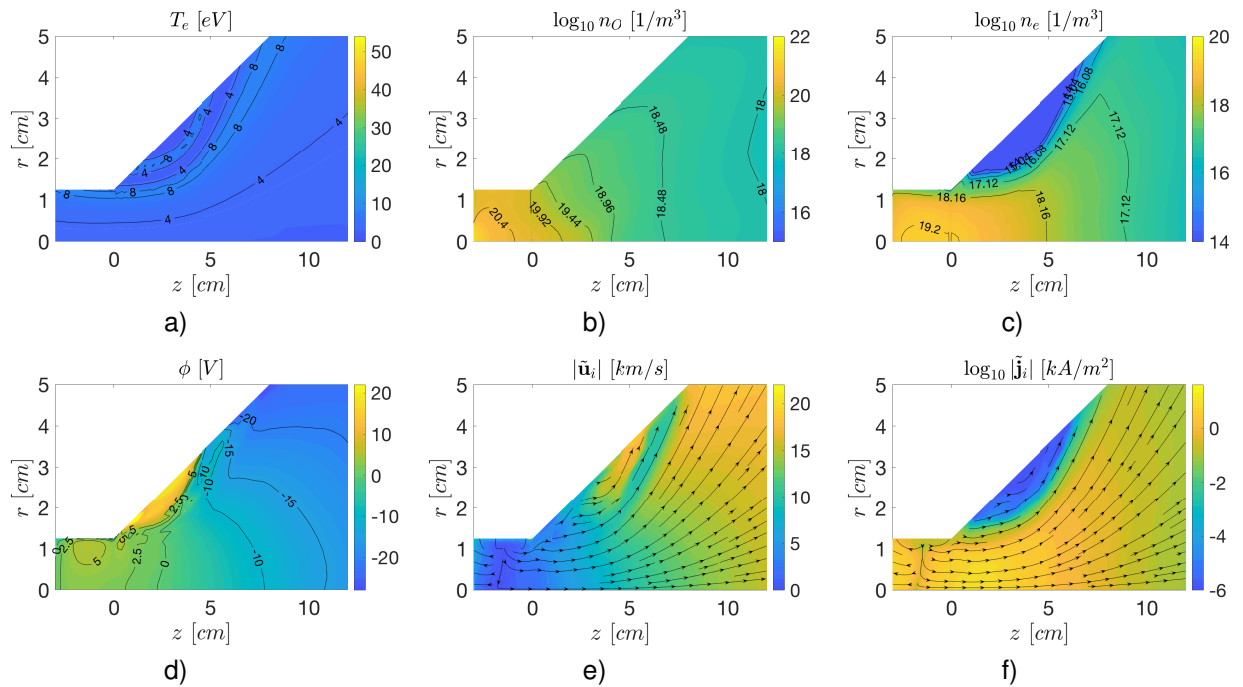


Figure 6: 2D maps of plasma magnitudes for O .

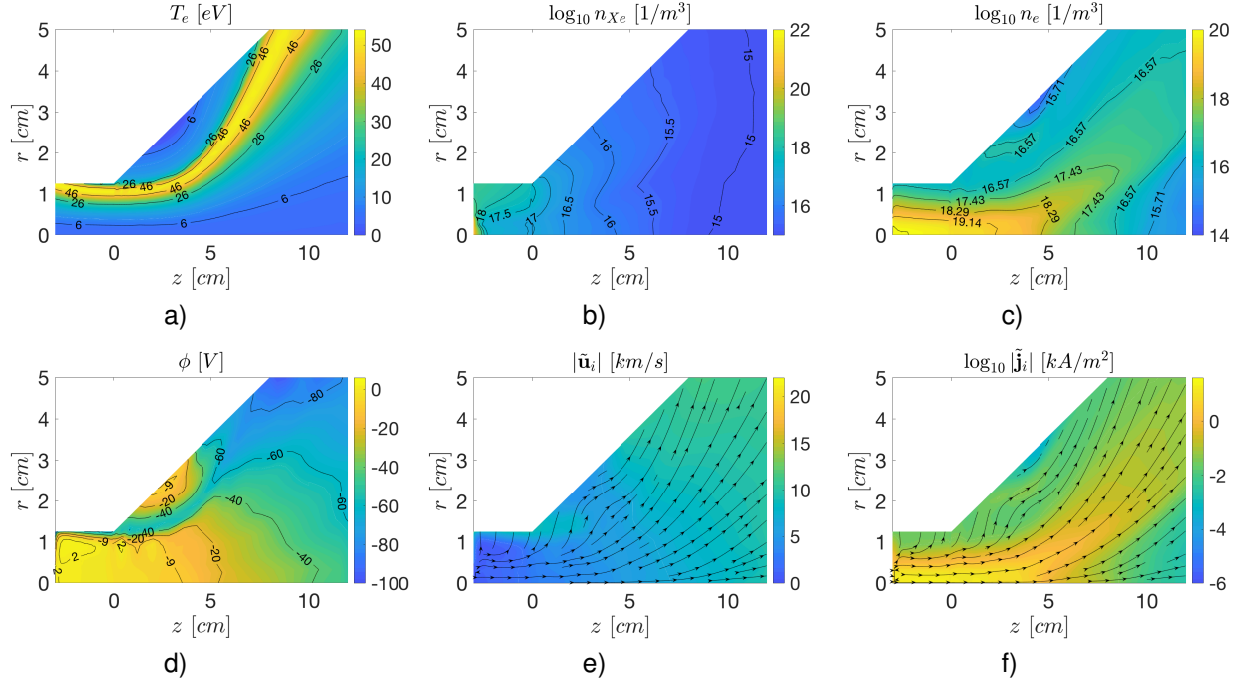


Figure 7: 2D maps of plasma magnitudes for Xe .

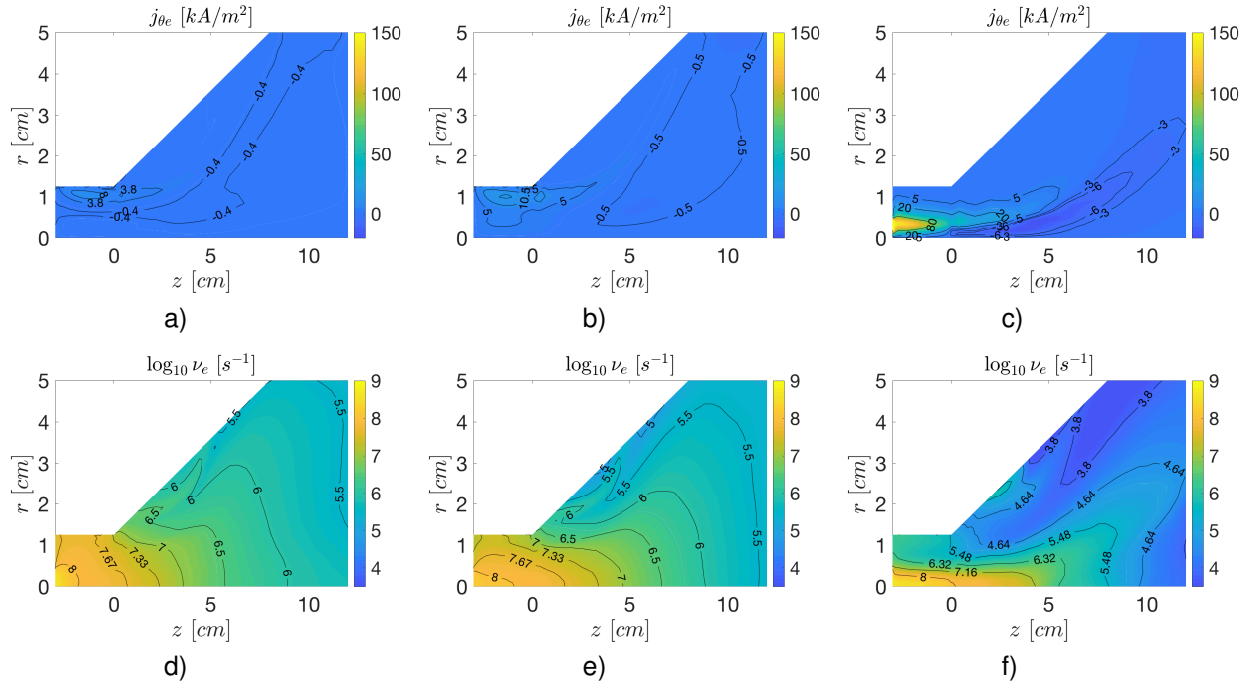


Figure 8: Electron azimuthal current density and total collision frequency for N_2 (first column), O (second column), and Xe (third column).

	$\langle T_e \rangle$ [eV]	F [mN]	η_u	η_{ene}	η_{disp}	η_F	η_p	ϵ_{wall}	ϵ_{inel} ($\epsilon_{ion} + \epsilon_{exc} + \epsilon_{diss}$)
N_2 -300W	4.84	2.82	0.20	0.16	0.40	0.013	0.40	0.15	0.11+0.53+0.05
O -300W	5.19	5.23	0.34	0.35	0.38	0.045	0.44	0.21	0.21+0.23
Xe -300W	25.35	8.02	0.97	0.45	0.24	0.104	0.36	0.41	0.07+0.07
N_2 -600W	5.37	5.38	0.38	0.20	0.32	0.024	0.42	0.16	0.10+0.50+0.04
O -600W	7.00	9.64	0.62	0.41	0.30	0.076	0.45	0.24	0.18+0.17
Xe -600W	46.98	11.34	0.98	0.45	0.24	0.108	0.37	0.50	0.03+0.02

Table 3: Performance indicators of a particular HPT05M configuration operated with N_2 , O and Xe .

corresponding particle formulation, while the one of electrons comes directly from the fluid formulation. In a plasma well ionized and evaluating the integral far downstream of the plume, the main contribution to the thrust is from the dynamic component of ions. The thrust efficiency is defined as

$$\eta_F = \frac{F^2}{2\dot{m}P_a}, \quad (\text{Eq. 15})$$

which measures the overall performance of the thruster.

Let define the ion mass flow towards the surface W1 as

$$\dot{m}_{i,W1} = \int_{W1} m_i n_i \mathbf{u}_i \cdot \mathbf{n} dS, \quad (\text{Eq. 16})$$

and the mass flows to W2 and W3, which, respectively, are $\dot{m}_{i,W2}$ and $\dot{m}_{i,W3}$, are analogous. The mass balance yields

$$\dot{m}_{i,W1} + \dot{m}_{i,W2} + \dot{m}_{i,W3} = \int_V S_{ion} dV, \quad (\text{Eq. 17})$$

where S_{ion} is the plasma production rate, and thus, $\dot{m}_{i,W1} + \dot{m}_{i,W2} + \dot{m}_{i,W3} = \dot{m}_{i,total}$ is the total plasma production. From the mass flows, $\dot{m}_{i,W3}$ is the useful for thrust, while $\dot{m}_{i,W1} + \dot{m}_{i,W2} = \dot{m}_{i,wall}$ is wall recombination. The quality of the plasma production inside the vessel are measured with the mass efficiency and production efficiency, which are, respectively,

$$\eta_u = \frac{\dot{m}_{i,W3}}{\dot{m}}, \quad \eta_{prod} = \frac{\dot{m}_{i,W3}}{\dot{m}_{i,total}}. \quad (\text{Eq. 18})$$

The first one, known also as propellant utilization, is the percentage of $\dot{m}_{i,W3}$ to the mass flow of propellant, and the second one is the percentage of $\dot{m}_{i,W3}$ to the total plasma production.

Integrating the energy equation for all species gives the power balance

$$P_a = P_{W1} + P_{W2} + P_{W3} + P_{inel}, \quad (\text{Eq. 19})$$

which is shown in Ref. [16]. The power absorbed is

$$P_a = \int_V Q_a dV, \quad (\text{Eq. 20})$$

and is distributed in: inelastic collisions P_{inel} , which is similar to P_a but volumetric integral of Q_e ; and energy flows P_{W1} , P_{W2} and P_{W3} , through, respectively, W1, W2 and W3, with P_{W1} defined as

$$P_{W1} = \int_{W1} \sum_s \left[\left(\frac{5}{2} T_s + \frac{1}{2} m_s u_s^2 \right) n_s \mathbf{u}_s + \mathbf{q}_s \right] \cdot \mathbf{n} dS, \quad (\text{Eq. 21})$$

and with analogous expressions for P_{W2} and P_{W3} . The energy efficiency is defined as

$$\eta_{ene} = \frac{P_{W3}}{P_a}, \quad (\text{Eq. 22})$$

i.e. power flow in the free surface, which is the useful one for thrust, and the inefficiencies are

$$\epsilon_{wall} = \frac{P_{W1} + P_{W2}}{P_a}, \quad \epsilon_{inel} = \frac{P_{inel}}{P_a}, \quad (\text{Eq. 23})$$

which correspond to wall and inelastic power losses. Finally, the operation of the magnetic nozzle is given by the dispersion efficiency

$$\eta_{disp} = \frac{F^2}{2\dot{m}_{i,W3} P_{W3}}. \quad (\text{Eq. 24})$$

This efficiency accounts for the velocity dispersion of plasma in the free surface, which comes from two contributions: divergence of the plume and degree of thermal-to-kinetic energy conversion. Notice that the combination of the partial efficiencies gives the overall one, $\eta_F = \eta_u \eta_{ene} \eta_{disp}$.

ACKNOWLEDGMENTS

The authors thank A. Domínguez-Vázquez and Filippo Cichocki, who provided counsel for the implementation of diatomic molecules collisions in HYPHEN. This work has been supported by the HIPATIA project, funded by the European Union's Horizon 2020 Research and Innovation Program, under Grant number GA870542. The contribution of E. Ahedo was supported by the Comunidad de Madrid (Spain), under Grant number Y2018/NMT-4750 PROMETEO-CM. Additional funding for a research stay of J. Zhou with F. Tacoogna at CNR was provided by the Ministerio de Education y Formación Profesional (Spain), under reference EST18/00221.

References

- [1] G. Parissenti, N. Koch, D. Pavarin, E. Ahedo, K. Katsonis, F. Scortecci, and M. Pesana. Non conventional propellants for electric propulsion applications. In *Space Propulsion 2010*, SP2010-1841086, San Sebastián, Spain, 2010.
- [2] K. Holste and et al. In search of alternative propellants for ion thrusters. In *34th International Electric Propulsion Conference, Hyogo-Kobe, Japan*, IEPC-2015-320, 2015.
- [3] V. Giannetti and et al. Electric propulsion system trade-off analysis based on alternative propellant selection. In *Space Propulsion Conference*, number SP2016-3125194, Rome, Italy, 2016. Association Aéronautique et Astronautique de France.
- [4] J. Szabo, M. Robin, S. Paintal, B. Pote, V. Hruby, and C. Freeman. Iodine propellant space propulsion. In *33th International Electric Propulsion Conference, Washington, USA*, IEPC-2013-311, 2013.
- [5] M. Tsay, J. Model, C. Barcroft, J. Frongillo, J. Zwahlen, and C. Feng. Integrated testing of iodine bit-3 rf ion propulsion system for 6u cubesat applications. In *35th International Electric Propulsion Conference, Atlanta, USA*, IEPC-2017-264, 2017.
- [6] Y. Nakagawa, H. Koizumi, H. Kawahara, and K. Komurasaki. Performance characterization of a miniature microwave discharge ion thruster operated with water. *Acta Astronautica*, 157:294 – 299, 2019.
- [7] R. Moloney and et al. Experimental validation and performance measurements of an ecr thruster operating on multiple propellants. In *36th International Electric Propulsion Conference, Vienna, Austria*, IEPC-2019-199, 2019.
- [8] A.J. Sheppard and J.M. Little. Scaling laws for electrodeless plasma propulsion with water vapor propellant. *Plasma Sources Science and Technology*, 29:045007, 2020.
- [9] D. Di Cara and et al. Ram electric propulsion for low earth orbit operation: an esa study. In *30th International Electric Propulsion Conference, Florence, Italy*, IEPC-2007-162, 2007.
- [10] k.D. Diamant. A 2-stage cylindrical hall thruster for air breathing electric propulsion. In *46th AIAA/ASME/SAE/ASEE*, 2010.
- [11] F. Romano and et al. Performance evaluation of a novel inductive atmosphere-breathing ep system. In *35th International Electric Propulsion Conference, Atlanta, USA*, IEPC-2017-184, 2017.
- [12] T. Andreussi, E. Ferrato, A. Piragino, G. Cifali, A. Rossodivita, and M. Andrenucci. Development and experimental validation of a hall effect thruster ram-ep concept. In *Space Propulsion Conference*, number SP2018-00431, Seville, Spain, 2018. Association Aéronautique et Astronautique de France.
- [13] T. Ziemba, J. Carscadden, J. Slough, J. Prager, and R. Winglee. High power helicon thruster. In *41th AIAA/ASME/SAE/ASEE Joint Propulsion Conference & Exhibit*, AIAA 2005-4119, 2005.
- [14] T. Ziemba, P. Euripides, J. Slough, R. Winglee, L. Giersch, J. Carscadden, T. Schnackenberg, and S. Isley. Plasma characteristics of a high power helicon discharge. *Plasma Sources Science and Technology*, 15:517, 2006.
- [15] C Charles, RW Boswell, R Laine, and P MacLellan. An experimental investigation of alternative propellants for the helicon double layer thruster. *Journal of Physics D: Applied Physics*, 41(17):175213, 2008.
- [16] Jiewei Zhou, Daniel Pérez-Grande, Pablo Fajardo, and Eduardo Ahedo. Numerical treatment of a magnetized electron fluid within an electromagnetic plasma thruster code. *Plasma Sources Science and Technology*, 28(11):115004, 2019.
- [17] A. Sánchez-Villar, J. Zhou, Mario Merino, and Eduardo Ahedo. Coupled plasma transport and electromagnetic wave simulation of an ecr thruster. *Plasma Sources Science and Technology*, accepted for publication.
- [18] Adrián Domínguez-Vázquez, Filippo Cichocki, Mario Merino, Pablo Fajardo, and Eduardo Ahedo. Axisymmetric plasma plume characterization with 2D and 3D particle codes. *Plasma Sources Science and Technology*, 27(10):104009, 2018. doi:10.1088/1361-6595/aae702.
- [19] Adrián Domínguez-Vázquez. *Axisymmetric simulation codes for Hall effect thrusters and plasma plumes*. PhD thesis, Universidad Carlos III de Madrid, Leganés, Spain, 2019.
- [20] Daniel Pérez-Grande. *Fluid modeling and simulation of the electron population in Hall effect thrusters with complex magnetic topologies*. PhD thesis, Universidad Carlos III de Madrid, Leganés, Spain, 2018.
- [21] J.M. Fife. *Hybrid-PIC Modeling and Electrostatic Probe Survey of Hall Thrusters*. PhD

- thesis, Massachusetts Institute of Technology, 1998.
- [22] F.I. Parra, E. Ahedo, M. Fife, and M. Martínez-Sánchez. A two-dimensional hybrid model of the Hall thruster discharge. *Journal of Applied Physics*, 100:023304, 2006.
- [23] Eduardo Ahedo, Sara Correyero, Jaume Navarro, and Mario Merino. Macroscopic and parametric study of a kinetic plasma expansion in a paraxial magnetic nozzle. *Plasma Sources Science and Technology*, 29(4):045017, 2020. doi:10.1088/1361-6595/ab7855.
- [24] E. Ahedo and V. de Pablo. Combined effects of electron partial thermalization and secondary emission in Hall thruster discharges. *Physics of Plasmas*, 14:083501, 2007.
- [25] F. Taccogna, S. Longo, and M. Capitelli. Plasma sheaths in Hall discharge. *Physics of Plasmas*, 12:093506, 2005.
- [26] M. Capitelli, C.M. Ferreira, B.F. Gordiets, and A.I. Osipov. *Plasma kinetics in atmospheric gases*. Springer, Berlin, Germany, 2000.
- [27] Y. Itikawa and A. Ichimura. Cross sections for collisions of electrons and photons with atomic oxygen. *Journal of Physical and Chemical Reference Data*, 19:637–651, 1990.
- [28] Y. Itikawa. Cross sections for electron collisions with nitrogen molecules. *Journal of Physical and Chemical Reference Data*, 35:31–53, 2006.
- [29] T. Tabata, T. Shirai, M. Sataka, and H. Kubo. Analytic cross sections for electron impact collisions with nitrogen molecules. *Atomic Data and Nuclear Data Tables*, 92:375–406, 2006.
- [30] T. Tabata, T. Shirai, M. Sataka, and H. Kubo. Erratum to “analytic cross sections for electron impact collisions with nitrogen molecules” [at. data nucl. data tables 92 (2006) 375-406]. *Atomic Data and Nuclear Data Tables*, 98:74, 2012.
- [31] Y. Wang, O. Zatsarinny, and K. Bartschat. B-spline r-matrix-with-pseudostates calculations for electron-impact excitation and ionization of nitrogen. *Physical Review A*, 89:062714, 2014.
- [32] S.S. Tayal and O. Zatsarinny. B-spline r-matrix-with-pseudostates approach for excitation and ionization of atomic oxygen by electron collisions. *Physical Review A*, 94:042707, 2016.
- [33] Lxcat database. <https://nl.lxcat.net>. Accessed: 2019-10-21.
- [34] L.C. Pitchford et al. Lxcat: an open-access, web-based platform for data needed for modeling low temperature plasmas. *Plasma Process and Polymers*, 14:1600098, 2017.
- [35] J.A. Bittencourt. *Fundamentals of plasma physics*. Springer, Berlin, Germany, 2004.